International Journal of Greenhouse Gas Control 99 (2020) 103082

Contents lists available at ScienceDirect

International Journal of Greenhouse Gas Control

journal homepage: www.elsevier.com/locate/ijggc

Effects of permeability on CO_2 dissolution and convection at reservoir temperature and pressure conditions: A visualization study

Widuramina Amarasinghe[a,b,*], Ingebret Fjelde[a,b], Jan-Åge Rydland[a], Ying Guo[a,b]

[a] NORCE Norwegian Research Centre AS, Stavanger 4021, Norway
[b] University of Stavanger, Stavanger 4036, Norway

ARTICLE INFO

Keywords:
Supercritical CO_2
Dissolution and convection
Realistic reservoir conditions
Visualization
Permeability

ABSTRACT

When CO_2 is injected into aquifers, CO_2 will dissolve into the water phase. CO_2 dissolution initiated by diffusion, will increase the density of the water phase and thereby commence the convective flow of CO_2. The objective of the presented work was to visually investigate the effects of permeability on the convective mixing of supercritical CO_2 with water at realistic reservoir conditions (pressure and temperature). This required construction of a high-pressure transparent Hele-Shaw cell that allowed visualization of CO_2 transport, and the development of experimental procedures.

To develop the high-pressure Hele-Shaw cell, stress/strain calculations and simulations were carried out to select the best building materials for realistic working pressure and temperature and required dimensions to study convection. Porous media of different permeabilities were prepared using glass beads of different sizes. The experiments were carried out at 100 bar and 50 °C using a deionized water solution with Bromothymol blue (BTB) as pH indicator.

In the constructed Hele-Shaw 2D-cell, the cell volume was formed by two glass plates separated by an adjustable spacer. In the present study, the cell thickness was 5.0 mm in the main part of the cell volume. The high-pressure Hele-Shaw cell has made it possible to investigate CO_2-dissolution and mixing with water at pressures and temperatures realistic for CO_2-storage reservoirs in a porous medium for the first time.

CO_2 mixing and finger initiation in the water phase without the presence of porous media was an instantaneous process. The rate for CO_2 dissolution and mixing with water was found to increase with increasing permeability. The CO_2 dissolution pattern was found to depend on the permeability. Fingering of CO_2-rich high-density water was observed with the highly permeable porous medium. Piston-like displacement was observed in lower permeable porous medium.

1. Introduction

Greenhouse gas emissions and global warming have become hot topics in the past few decades. The Paris Agreement has insisted on keeping the global temperature rise below 2 °C within this century (United Nations, 2015). Carbon capture and storage (CCS) to reduce the carbon emissions is proposed as a key element to achieve the targets of the Paris agreement (IPCC, 2005). To establish a proper CCS value chain, an improved understanding of CO_2 storage and utilization mechanisms is important. Deep saline aquifers have higher storage capacity (Celia et al., 2015; Freund and Ormerod, 1997). Due to the high cost for CO_2 storage, CO_2 utilization also been considered. Hence significant attention has been given to CO_2 injection into oil fields with the intention of enhancing the oil recovery (EOR) (Brock and Bryan, 1989; Holm, 1982; Sohrabi et al., 2009). Through CO_2 EOR more financial viability towards CO_2 storage can be achieved by increasing the oil production and using existing infrastructure (Kuuskraa et al., 2013; Roefs et al., 2019).

When CO_2 is injected into aquifers, CO_2 will dissolve into the water phase (Lin et al., 2008). CO_2 can also be trapped by structural trapping, residual trapping, and mineral trapping (Zhang and Song, 2014; Bachu, 2008). Solubility trapping is one of the key mechanisms for long term CO_2 storage and EOR. At reservoir conditions (high pressure and high temperature), supercritical CO_2 (sCO_2) will have a lower density than the other fluids present. CO_2 dissolution into water initiated by diffusion, will increase the density and thereby accelerate convective mixing of CO_2. This gravity-driven process will contribute to CO_2 storage by accelerating the CO_2 dissolution (Zhao et al., 2011). Experimental

* Corresponding author at: NORCE Norwegian Research Centre AS, Stavanger 4021, Norway.
E-mail address: widuramina@norceresearch.no (W. Amarasinghe).

https://doi.org/10.1016/j.ijggc.2020.103082
Received 25 November 2019; Received in revised form 27 May 2020; Accepted 28 May 2020

Nomenclature

λ	Wavelength,mm
ρ_{CO2}	Density of CO_2,kg/m^3
ρ_{water}	Density of water,kg/m^3
$\rho_{(water+CO_2)mix}$	Density of water + CO_2 mixture,kg/m^3
$\Delta\rho$	Density increase of the fluid due to CO_2 dissolution $\rho_{(water+CO2)mix}$, kg/m^3
τ	Dimensionless time
Φ	Porosity
μ	Dynamic viscosity of the fluid,kg/(s·m)
b	Cell thickness,m
D	Molecular diffusion co-efficient of CO_2 in the fluid,m^2/s
g	Acceleration of gravity,m/s^2
H	Test height of porous medium,m
k	Permeability of the porous medium,m^2
Ra	Rayleigh number
$Ra_{critical}$	Critical Rayleigh number
sCO_2	Super Critical CO_2
t_{4cm}	Time taken CO_2 to reach at 4 cm depth, min

Definition

CO_2convection Water is convecting and it circulate the CO_2 with it

investigation of the CO_2 dissolution process in different types of porous media with different fluid systems and at realistic reservoir conditions (pressure and temperature) is important for further development of technology and simulation models.

Many experimental studies have been conducted to investigate convection dissolution of CO_2 inside porous media (Neufeld et al., 2010; Tsai et al., 2013; Agartan et al., 2015; Vosper et al., 2014; Fang and Babadagli, 2016; Lv et al., 2016, 2017, Zhao et al., 2011; Mahmoodpour et al., 2019; Wang et al., 2016; Liyanage et al., 2017; Amarasinghe et al., 2018; Teng et al., 2017). Those experimental studies were conducted either in 2D Hele-Shaw cells or 3D cylindrical cells with glass beads or sand packs as porous media. To visualize the dissolution of CO_2 in another fluid by optical methods, 2D Hele-Shaw cells packed with glass beads have been used. 3D cylindrical cells with sand packs have been used to measure the mass transfer rate of CO_2 dissolution into another fluid along with PVT measurements using non-optical methods.

Hele-Shaw cells are used to visualize the flow so that 3D effects can be neglected. i.e. flow inside will be mathematically analogous to a 2D effect (Hartline and Lister, 1977). A Hele-Shaw cell is made with two parallel flat plates are separated by a small gap (generally less than 2 mm) (Soroush et al., 2012). Width and height can be any size depending on the requirement, but typically it has not exceeded 50 cm. The thickness of a Hele-Shaw cell is critical due to a few reasons; (1) To obtain an analogy with 2D effects only (2) The thickness is good enough for the light rays to go through so a clear visualization can be observed. The theory says that the Rayleigh number (Ra) (see Eq. (1)) which is a dimensionless number of the ratio between free convection to diffusion, should be equal or greater than $Ra_{critical}$, $4\pi^2$ (39.47), for the natural convection to become substantial (Faisal et al., 2015; Lindeberg and Wessel-Berg, 1997):

$$Ra=\frac{\Delta\rho gkH}{\mu D\Phi} \quad (1)$$

Where, $\Delta\rho$ is the density increase of water due to CO_2 dissolution, g is the acceleration of gravity, k is the permeability of the porous medium, H is the height of the porous medium, μ is the dynamic viscosity of water, D is the molecular diffusion coefficient of CO_2 in water and Φ is the porosity of porous medium.

The relationship between permeability and the 2D cell thickness (when porous medium is not present) is given by the Eq. (2) where b is the cell thickness (Faisal et al., 2015).

$$k=\frac{b^2}{12} \quad (2)$$

Usage of solutions with pH indicators (Faisal et al., 2015; Kneafsey and Pruess, 2011; Mojtaba et al., 2014; Thomas et al., 2015; Teng et al., 2018; Vosper et al., 2014; Mahmoodpour et al., 2019; Vreme et al., 2016; Outeda et al., 2014; Taheri et al., 2018; Amarasinghe et al., 2018) and projection methods such as Schlieren method (Khosrokhavar et al., 2014; Thomas et al., 2015; Tang et al., 2019) are common techniques to visualize fluid flow/mixing inside Hele-Shaw cells.

Generally, 3D cells are used when a closed system is required to investigate the CO_2 dissolution processes, especially when quantitative data is required such as pressure decay and total CO_2 mass dissolution. These 3D cells are made with special grade steel or titanium in a cylindrical shape (Emami-Meybodi et al., 2015). Some 3D cells contain a narrow transparent glass to observe convective dissolution of CO_2 into fluids. High-end technologies like X-ray and MRI (Magnetic Resonance Imaging) technologies have been used to visualize the CO_2 process inside the cell (Zhao et al., 2011; Lv et al., 2016, 2017).

Many experiments have been conducted at atmospheric conditions using surrogate fluids to mimic sCO_2 and other liquids (water, brine, oil) (Neufeld et al., 2010; Soroush et al., 2012; Taheri et al., 2012; Tsai et al., 2013; Agartan et al., 2015; Wang et al., 2016; Liyanage et al., 2017; Teng et al., 2017). A mixture of methanol and ethylene glycol is a common surrogate fluid to mitigate sCO_2. The main purpose of surrogate fluids is to lower the pressure and temperature condition to ambient conditions. Normally the surrogate fluids are selected to match the density profile of CO_2 and water, and the mixture of CO_2 and water. The density profiles may different from the actual values of CO_2 and water which depend on the temperature and pressure. Even though density profile matches, viscosity profiles may differ from the actual values which depend on the fluid concentrations, temperature, and pressure (Emami-Meybodi et al., 2015; Neufeld et al., 2010). Table 1 shows a summary of vertical flow visualization experiments published in literature where experiments have been conducted at ambient conditions with and without porous medium using surrogate fluids to mimic CO_2-transport.

A handful of studies have conducted experiments at high-pressure conditions to demonstrate sCO_2 dissolution into another fluid (without the presence of porous medium) (Teng et al., 2018; Khosrokhavar et al., 2014; Song et al., 2003; Zhao et al., 2011; Tang et al., 2019). Only a few studies have been carried out using actual CO_2 with the presence of porous medium (Amarasinghe et al., 2018; Mahmoodpour et al., 2019; Vosper et al., 2014), but in all those experiments CO_2 was a gas phase. Table 2 shows a summary of the CO_2 flooding experiments with visualization that have been published in the literature. The summary includes experimental studies conducted to visualize and acquire data for CO_2 convective and gravity-driven dissolution into another fluid with or without porous medium.

Since experiments with visualization of CO_2 dissolution into fluid phases in porous medium at reservoir temperature and pressure conditions were not available (see Table 2), construction of a high-pressure transparent Hele-Shaw cell was required. The objective of the presented work was to design and construct a high-pressure transparent Hele-Shaw cell to investigate the effects of permeability on the mixing of sCO_2 with water by convective flow at realistic reservoir conditions (pressure and temperature).

Table 1
Summary of vertical flow visualization experiments published in the literature where the experiments were conducted at ambient conditions using surrogate fluids to mimic sCO_2.

Reference	Experimental setup description / type	Mimic fluids	Porous medium	Visualization method
(Neufeld et al., 2010)	Hele-Shaw cell	MEG and Water	Glass beads	Chemical dye added to brine solution / Camera
(Sorousb et al., 2012) and (Taheri et al., 2012)	Hele-Shaw cell	Water / Brine	No porous medium	Chemical dye added to brine solution / Camera
(Tsai et al., 2013)	Hele-Shaw cell	Water / Propylene glycol	Glass beads	Shadowgraph imaging by camera
(Agartan et al., 2015)	2D test tank	Water / Propylene glycol	Sand	Food dye solution / Camera
(Teng et al., 2017)	Cylindrical packed bed	Water / $MnCl_2$ / D_2O / Brine	Plastic sands and glass beads	MRI imaging
(Wang et al., 2016)	Cylindrical packed bed	Mixture of methanol and ethylene glycol + NaI / NaCl	Melamine resin particles	X-ray CT scanning
(Liyanage et al., 2017)	Spherical bowl	Mixture of methanol and ethylene glycol and Brine (Water)	Glass beads	X-ray CT scanning

2. Method

2.1. Development of high-pressure Hele-Shaw cell

The high-pressure Hele-Shaw cell was developed using stainless duplex steel (with EN1.4462 quality to avoid possible corrosion by CO_2) and borosilicate glass (to enhance the optical visualization from outside). Different calculations and stress/strain simulations were carried out using Autodesk® Inventor HSM™ Ultimate software to select the best building materials for realistic working pressure and temperature. The 2D cell was designed for maximum working conditions of 150 bar and 100 °C. The test cell was pressure-tested at 225 bar and 25 °C. The test cell consists of several units, which are assembled to construct the final cell. The cell volume was formed by two glass plates separated by an adjustable spacer. These two METAGLAS® metal fused sight glasses were prepared of borosilicate glass fused into a steel ring. A steel outer shell was used to reinforce the glass cell to overcome the pressure forces inside the cell. A cross-section of the cell is shown in Fig. 2 while a 3D sketch of the cell is shown in Fig. 1. The front view of the real cell with insulation is shown in Fig. 3. One of the main limitations for working pressure and cell dimensions was the glass in the sight disks used for visualization.

There is a special pressure release design between glass and steel of the sight disk to reduce the stress level. A specially designed filter module of shaped glass filter (pore size $10-16\,\mu m$) plate was placed at the inlet and outlet to avoid penetrating of the glass beads away from the test volume (see Fig. 2 and Fig. 1). The location of the gas introduction was placed in the middle of the top filter module unit as shown in Fig. 2. The diameter of the test volume is 200 mm while the sight disk glass diameter was 100 mm. The thickness is 5.0 mm between glass sight disks. The total test volume was calculated to be 101 ml neglecting the pore volume of the top and bottom filters.

The force on the sight disk was calculated as 0.7 MN at test pressure (225 bar) and 0.47 MN at maximum working pressure (150 bar). Yield stress (450 MPa), tensile stress (650 MPa), and respective safety factors (1.5 and 2.4 respectively) for steel were selected (Trykkbeholderkomite, 1986). To decide the optimum working pressure of the cell, the maximum allowable stress on the walls was calculated using equations Eqs. (3.a) and (3.b).

$$\text{Maximum allowable stress} = \min\left\{\frac{\text{Yield stress for steel}}{\text{Yield safety factor}}, \frac{\text{Tensile stress for steel}}{\text{Tensile safety factor}}\right\} \tag{3.a}$$

$$\text{Maximum allowable stress} = \min\left\{\frac{450\,\text{MPa}}{1.5}, \frac{650\,\text{MPa}}{2.4}\right\} = 271\,\text{MPa} \tag{3.b}$$

The simulated stress values for both test and maximum working pressure for different areas of steel and sight disk are shown in Figs. 4 and 5. The maximum stress value achieved from the simulations at 150 bar was 236.7 MPa (shown in Fig. 4-b), which is lower than the calculated maximum allowable stress of 271 MPa in Eq. (3.b).

The temperature was controlled by a heating cable wrapped around the cell connected to a heating controller. Two sensors, one to sense the actual body temperature of the cell and the other to sense the temperature under the heating cable was used. Thick insulation around the cell except covering the sight disk was used to prevent heat loss.

2.2. Materials

Bromothymol blue (BTB) pH indicator solution (0.004 wt% BTB with 0.01 M NaOH prepared in deionized water) of pH around 8 was used as the water phase. The BTB is blue above pH = 7.6 and yellow below pH = 6.5, and green between these pH-values (De Meyer et al., 2014). When CO_2 is dissolved in water, the pH will be reduced due to the release of H^+ ions (see Eqs. (4.a)-(4.c)) (Thomas et al., 2015).

Table 2
Summary of CO_2 flow visualization experiments stated in literature with and without porous medium.

Reference	Experimental setup description	Fluids	Porous medium	Conditions	Visualization method
(Amarasinghe et al., 2018)	Hele-Shaw cell	CO_2 / Water	Glass beads	10 bar / Ambient temperature	pH dye (Bromothymol Blue – BTB)
(Mahmoodpour et al., 2019)	Hele-Shaw cell	CO_2 / Brine	Glass beads	40 bar / 50 °C	pH dye (Bromocresol Green - BG)
(Vosper et al., 2014)	Hele-Shaw cell	CO_2 / Water	Glass beads	Ambient conditions	pH dye / Camera
(Faisal et al., 2015)	Hele-Shaw cell	CO_2 / Water	No porous medium	Ambient conditions	pH dye (BG)
(Lu et al., 2017)	Hele-Shaw cell	CO_2 / Brine	No porous medium	Ambient pressure / 22–45 °C	pH dye (Bromocresol purple - BP) / Back luminance light / High speed Camera
(Mojtaba et al., 2014)	Hele-Shaw cell	CO_2 / Brine	No porous medium	Ambient conditions	pH dye (litmus powder) / Camera
(Taheri et al., 2018)	Hele-Shaw cell	CO_2 / Water	No porous medium	Ambient conditions	pH dye (BG) / Camera
(Thomas et al., 2015, 2018)	Hele-Shaw cell	CO_2 / Water and brine	No porous medium	Ambient conditions	pH dyes (BP and BG) / Schlieren method
(Outeda et al., 2014)	Hele-Shaw cell	CO_2 / Water	No porous medium	1.5 – 5 bar / 25 °C	pH dye (BG) / Camera
(Vreme et al., 2016)	Hele-Shaw cell	CO_2 / Water	No porous medium	6 bar / 25 °C	pH dye / Camera
(Kneafsey and Pruess, 2010, 2011)	Hele-Shaw cell	CO_2 / Water and atmospheric air (380 ppm CO_2) / water	No porous medium	40 bar / Ambient temperature	pH dye (BG) / Camera
(Teng et al., 2018)	Hele-Shaw cell	CO_2 / Brine	No porous medium	150 bar / 80 °C	pH dye (BG) / Camera
(Tang et al., 2019)	Hele-Shaw cell	CO_2 / Brine	No porous medium	200 bar / 80 °C	Micro-schlieren method
(Khosrokhavar et al., 2014)	Hele-Shaw cell	CO_2 / Water, CO_2 / Oil	No porous medium	64 – 84 bar / 39 °C	Schlieren method
(Song et al., 2003)	High-pressure cell	CO_2 / Water	No porous medium	50 – 125 bar / 0 – 15 °C	Mach-Zehnder Interferometry
(Fang and Babadagli, 2016)	3D test tank	Oil / Solvent	Glass beads	Ambient conditions	Fluorescence dye / High-speed Camera
(Lv et al., 2016, 2017)	3D high-pressure cell	CO_2 / Brine	Feldspar, Quartz, and Dolomite	8 bar / 40 °C	X-Ray CT scanning
(Zhao et al., 2011)	3D high-pressure cell	CO_2 / n-Decane	Glass beads	85 bar / 40 °C	MRI imaging

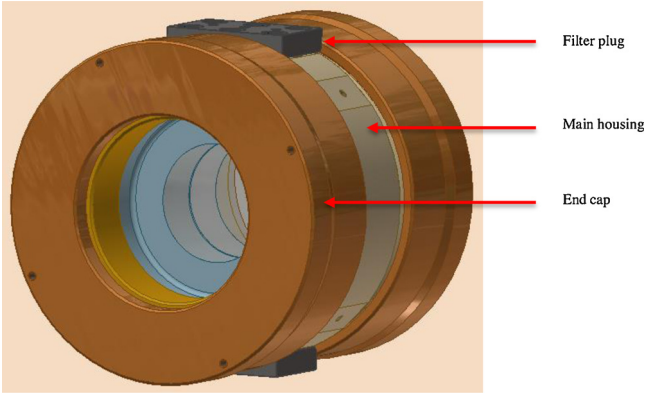

Fig. 1. 3D sketch of the high-pressure Hele-Shaw cell.

$$CO_2(g) \rightleftharpoons CO_2(aq) \quad (4.a)$$

$$CO_2(aq) + H_2O \rightleftharpoons H^+ + HCO_3^- \quad (4.b)$$

$$HCO_3^- \rightleftharpoons H^+ + CO_3^{2-} \quad (4.c)$$

Hydrophilic micro glass beads (SigmundLindner, 2020) of different diameters were used to prepare porous media of different permeabilities (500 mD, 4 D, 40 D, and 76 D). Fig. 6 shows the cumulative particle size distribution of the glass beads. The permeabilities of the bead packs were determined by waterflooding of packed glass bead tubes.

2.3. Experimental procedure

The experimental set-up with the high-pressure Hele-Shaw test cell is shown in the piping and instrumentation diagram (P & ID) (see Fig. 7). A back-pressure regulator was included in the set-up to avoid sudden developments of high-pressures inside the cell. CO_2 was introduced from a piston cell. A digital manometer was connected directly into the 2D cell to get an accurate reading of the absolute pressure.

The cell was filled manually with a known volume of pre-heated (50 °C) BTB solution. Then, dry glass beads were gradually added from the top of the cell to achieve an even distribution in the solution. When the desired level of porous medium was reached, small external vibration was applied to the cell by using a plastic hammer to ensure the beads were evenly arranged. Any water was above the porous medium, was sucked out using a syringe. After placing the filter module on the top of the cell, the cell was left for approximately half an hour to make sure that the packing has even out, and the temperature has stabilized (confirmed from a thermal image).

The CO_2 piston cell was first filled to 80 bar, and it was then heated to 50 °C. After the gas expansion, the piston cell was pressurized to 105 bar. A thermal image was taken by a FLUKE® Ti25 thermal imaging camera to make sure that the 2D cell was at a stable temperature. Around a 3 °C temperature gradient from the edge of the glass to the center of the glass was observed (see Fig. 8).

The fine valve (a needle valve with a regulating stem tip) connected to the CO_2 piston cell (see Fig. 7), was opened slowly to allow CO_2 flow into the 2D cell to avoid movement of glass beads. The Quizix pump was used to regulate the pressure to 100 bar. When the pressure was increased, a drop in the water and glass beads level was observed due to the liquid invasion into the pore space of the bottom filter and better packing of the beads. The Quizix pump was set in constant pressure mode to maintain constant pressure and to compensate for the reduction in pressure due to the dissolution of CO_2 into the water phase.

The visualization observations were carried out using a Nikon D5200 camera with an interval timer shooting. ImageJ open source software (Rueden et al., 2017) was used to analyze the CO_2 front movement in the images. There is a color difference in each experimental case with porous media due to the difference in glass beads sizes which leads to different light penetration/retroreflection (Héricz et al., 2017).

The set of experiments carried out is shown in Table 3 along with permeability for each porous medium with estimated Ra number. Table 4 shows the data used to estimate the Ra number for each experimental case. Different porous media heights were used in each case to maximize the visualization of CO_2 transport inside the porous media. To generalize all the experiments, experiment packing size were considered as 0.04 m.

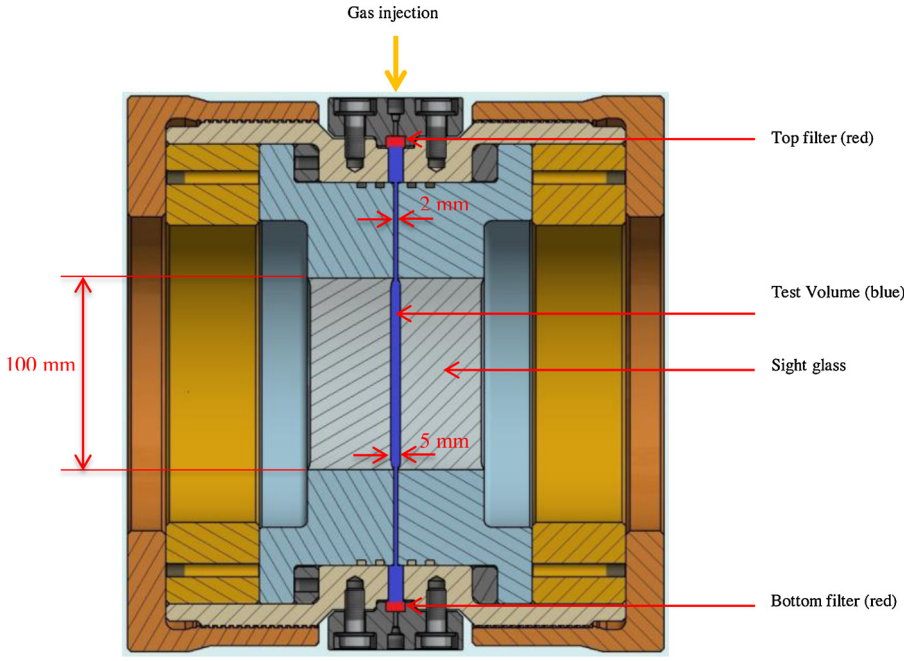

Fig. 2. Cross-section of the high-pressure Hele-Shaw cell.

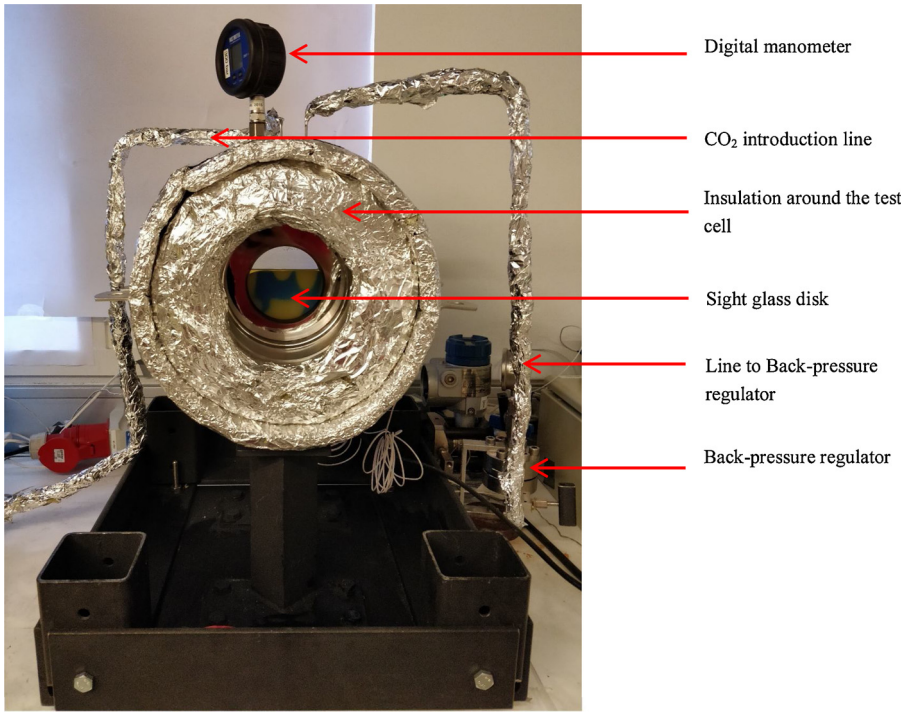

Fig. 3. Front view of the actual experiment setup.

3. Results and discussion

The constructed high-pressure Hele-Shaw cell has made it possible to investigate CO_2-dissolution and mixing with a water phase at pressures and temperatures realistic for reservoirs with CO_2-storage.

3.1. Visual observations of CO_2 dissolution into the water without porous medium

When CO_2 was introduced into the cell with the water phase but without any porous medium, sudden development of CO_2 fingering was observed. The fingers were observed to merge with time. The fingers were growing downwards due to the gravity-driven mechanism (see Fig. 9). Due to the presence of the high-pressure CO_2, the dissolution process was very fast. The whole process was finished in less than 1 min (the color of pH-indicator was completely changed from blue to yellow) while the time taken for CO_2 to reach a depth of 4 cm (t_{4cm}) was measured to be 25 s. Clear distinguishable fingers were observed up to 17 s from the start of the process. Four fingers per 1 cm width were calculated which were transformed to wavelength (λ) of 2.5 mm. In this case Ra number ($6{\cdot}10^6$) is very large compared to $Ra_{critical}$ which implies that the natural convection was more influential without the presence of

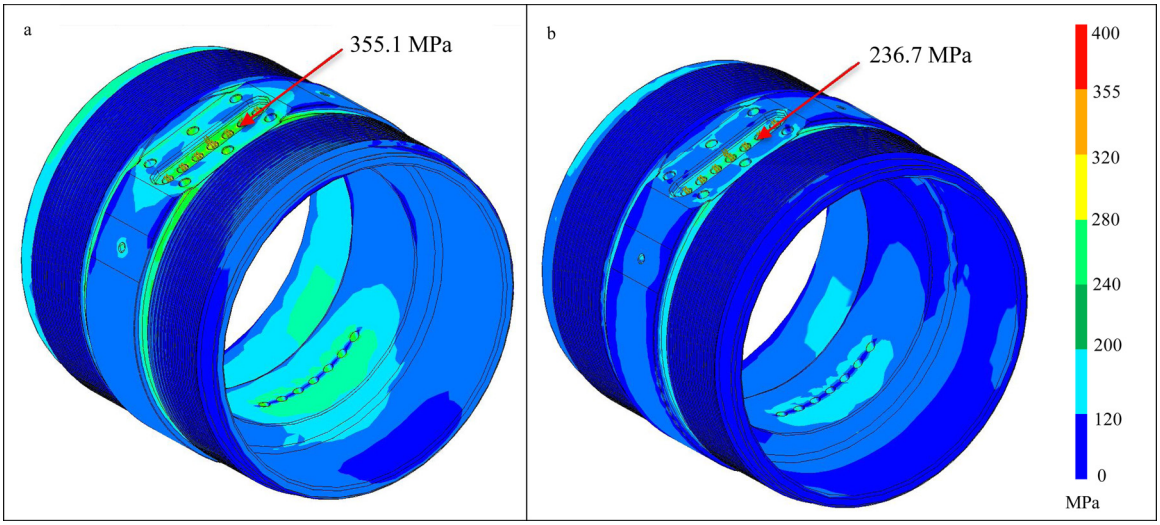

Fig. 4. Stress-analysis simulations carried out for the steel housing of the test cell.
(a) At test pressure of 225 bar (b) At maximum working pressure of 150 bar.

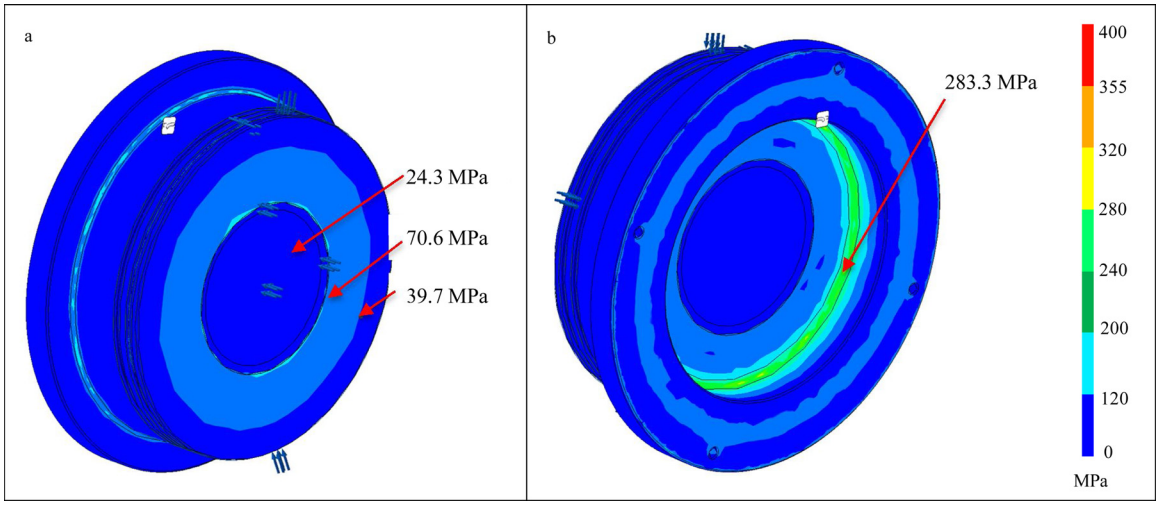

Fig. 5. Stress-analysis simulations carried out for the sight-disk at a maximum working pressure of 150 bar.
(a) From the pressurized-side (b) From the atmospheric-side.

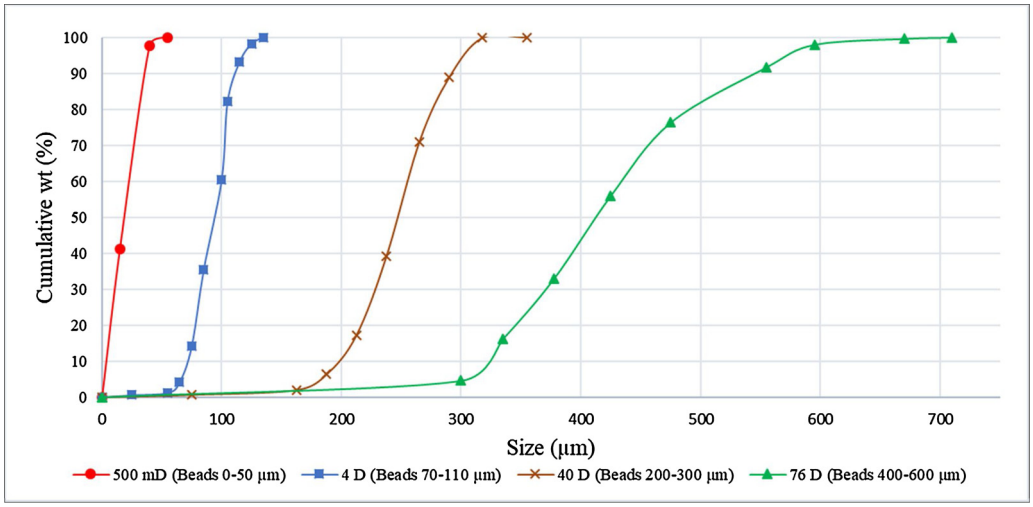

Fig. 6. Cumulative particle size distribution of the glass beads.

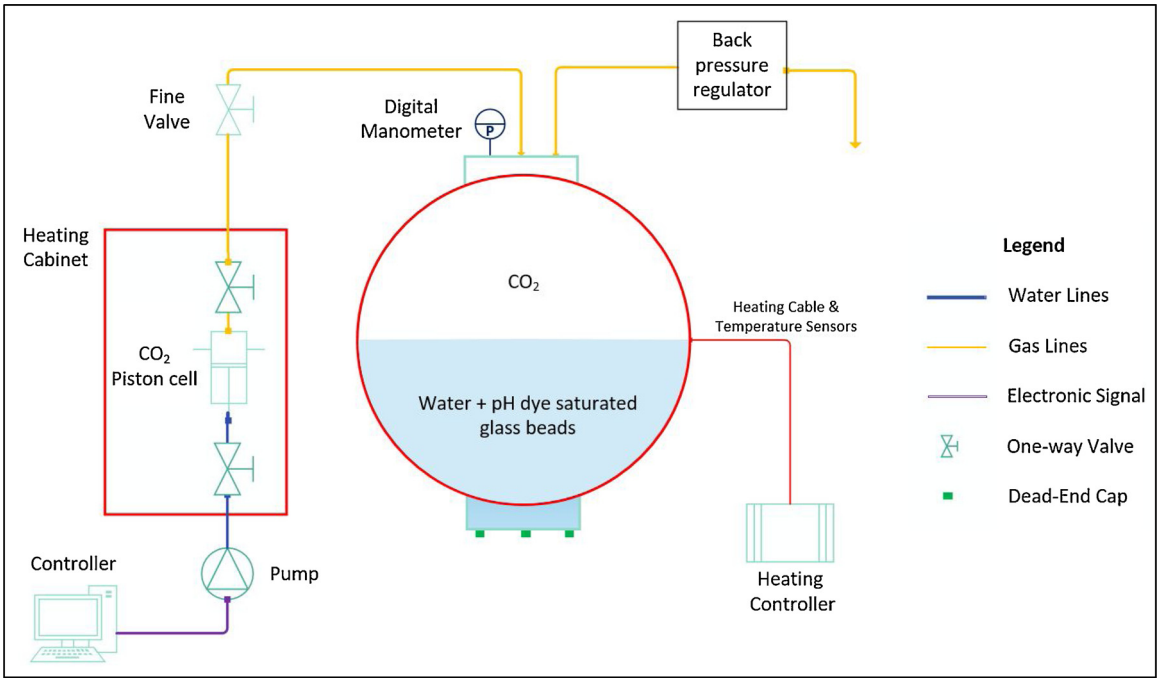

Fig. 7. Piping and instrumentation (P & ID) diagram of the experimental setup.

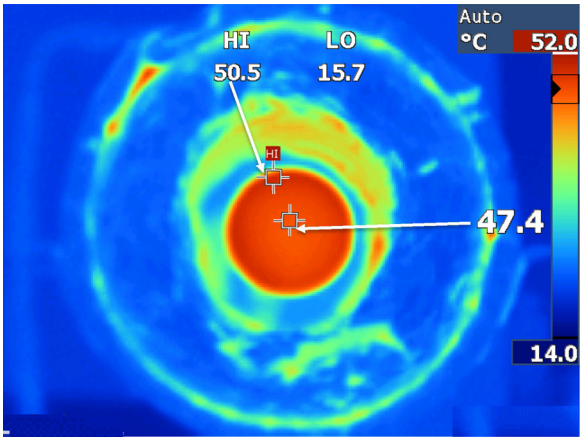

Fig. 8. Thermal image of the heated cell before introduction of CO_2.

Table 3
Set of experimental cases with CO_2/water at 100 bar and 50 °C.

Test no:	Porous medium (Glass beads) size range (μm)	Estimated permeability	Ra Number	Results
1	No porous medium	$2.11{\cdot}10^6$ D**	$6{\cdot}10^6$	Fig. 9
2	0 – 50	500 mD*	4	Fig. 10
3	70 – 110	4 D*	30	Fig. 11
4	200 – 300	40 D*	290	Fig. 12
5	400 – 600	76 D*	545	Fig. 13

* Determined in waterflooding of packed tubes.
** Calculated from Eq. 2.

porous medium. In this study, the CO_2 dissolution into the water phase was very fast compared to the studies in the literature where CO_2/water systems without the presence of porous medium were used (Faisal et al., 2015; Lu et al., 2017; Thomas et al., 2018). Experiments carried out by Amarasinghe et al. (2018) also have shown similar results with CO_2 dissolution at a comparatively lower rate compared to this present study. Even though in that study N_2 was used to pressurize the Hele-Shaw cell at 10 bar before introducing CO_2, they observed that it only took 4 min for CO_2 to reach the bottom of the cell (8 cm).

Table 4
Parameters for Ra number calculation.

Parameter	Value**	Units
ρ_{water}	988.05	kg/m^3
ρ_{CO2}	384.67	kg/m^3
$\rho_{(water+CO2)mix}$	1002.8 (Hebach et al., 2004; Efika et al., 2016)	kg/m^3
Δρ	14.75	kg/m^3
D	$3.643{*}10^{-9}$ (Cadogan et al., 2014)	m^2/s
H	0.04	m
g	9.81	m/s^2
μ	0.0005474	kg/s·m
φ	0.4 (Average)	–
b	5	mm

** Obtained at 50 °C/100 bar.

3.2. Effects of permeability for the CO_2 dissolution into water-saturated porous media

Introduction of CO_2 into water-saturated porous media of different permeabilities was studied visually. Piston-like displacement was observed in the lowest permeable porous medium, 500 mD (see Fig. 10). In the 4 D porous medium, an uneven piston-like displacement was observed. The growth of the CO_2 front was observed as piston-like (similar to 500 mD) until 275 min. Then CO_2 front became unstable and moved downwards. (see Fig. 11). With the further increment of the permeability, the number of fingers per unit width increased (see Figs. 12 and 13). At the initial stage many small fingers were observed in 76 D porous medium (see t = 3 min and t = 8 min. in Fig. 13). With time, the small fingers with a smaller wavelength (λ) merged, and much larger fingers with larger wavelengths (λ) were created.

The Ra numbers for 500 mD and 4 D porous media (4 and 30 respectively) are below the $Ra_{critical}$ (39.47) while the Ra number for higher permeability porous media is larger than $Ra_{critical}$. This explains the piston-like displacement in 500 mD and 4 D porous media and the finger-like convection flow in more permeable porous media. The flow

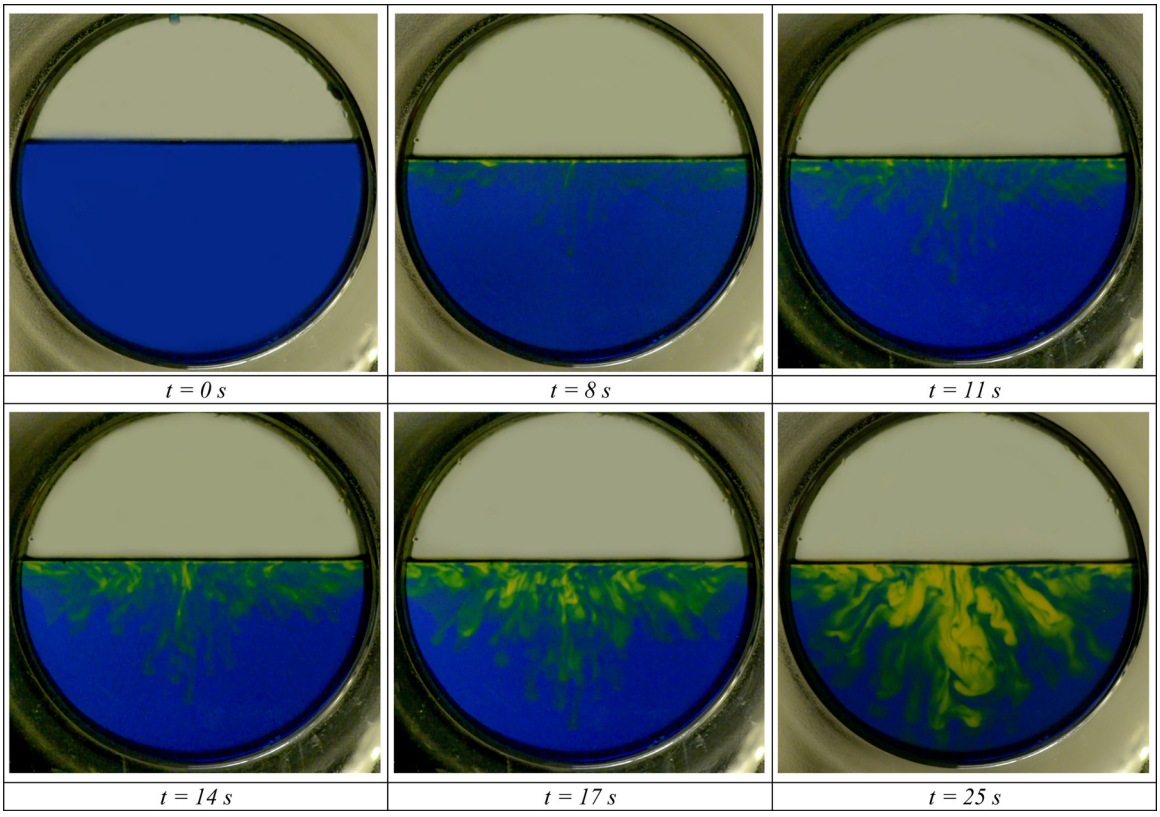

Fig. 9. Case 1; CO_2/Water system without porous medium.

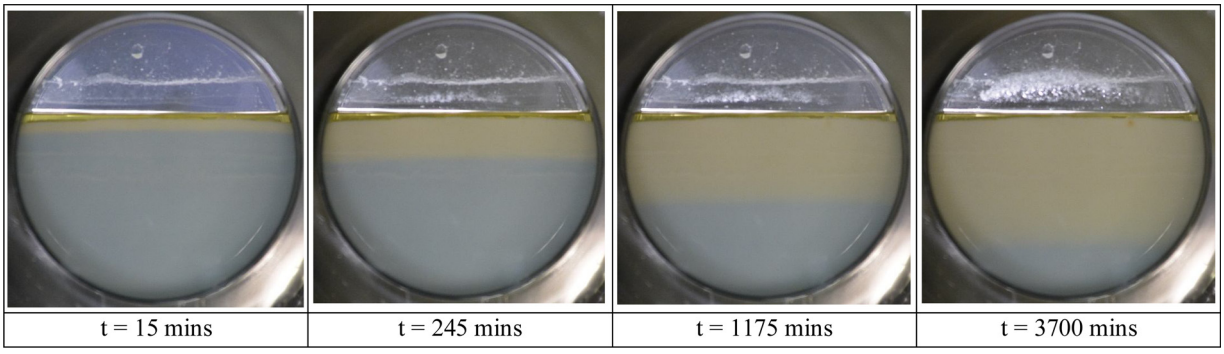

Fig. 10. Case 2; CO_2/Water system with porous medium with the permeability of 500 mD (0-50 μm).

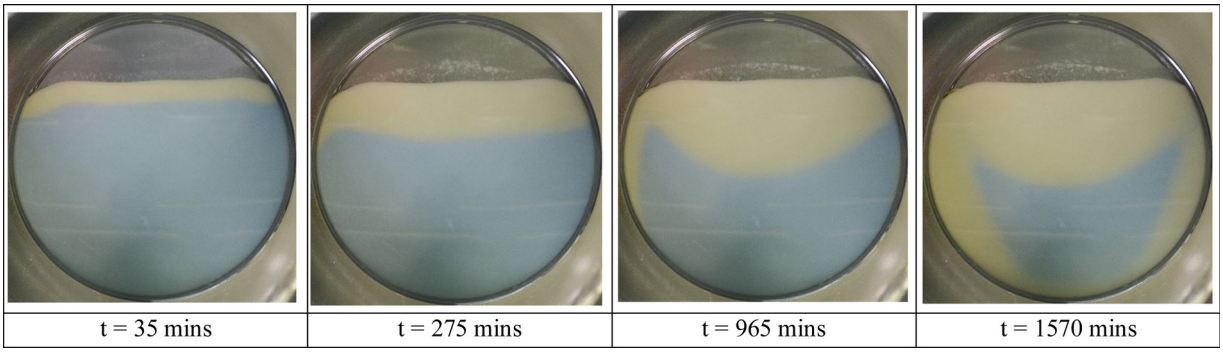

Fig. 11. Case 3; CO_2/Water system with porous medium with the permeability of 4 D (70-110 μm).

in 500 mD porous medium was diffusion dominated. It has been observed that in porous media with higher permeability (4 D, 40 D, and 76 D), the initiation of CO_2 dissolution was diffusion dominated. As seen in Fig. 11 t = 35 min, Fig. 12 t = 25 min, Fig. 13 t = 3 min., a small band of CO_2 dissolution was observed where diffusion of CO_2 occurred. Due to the density and viscosity changes of CO_2/water mixture with time, instability occurred which lead to flow downwards.

Fig. 14 shows the development of the CO_2 front (length) downwards

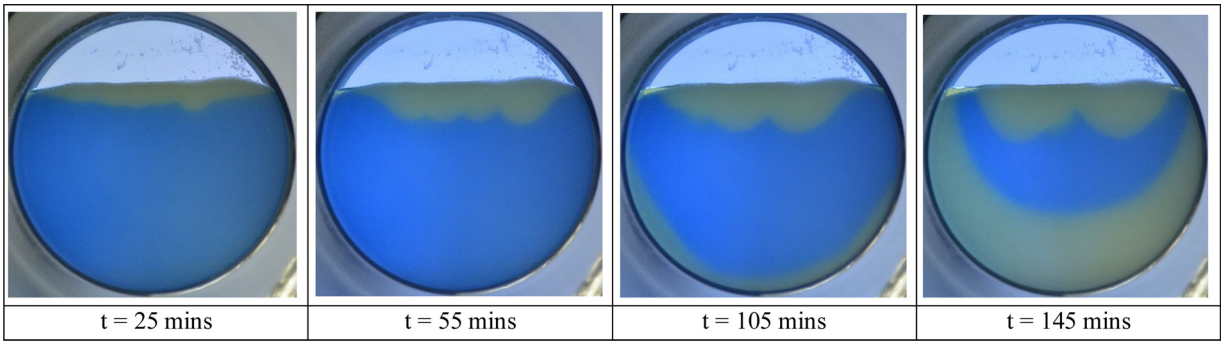

Fig. 12. Case 4; CO_2/Water system with porous medium with the permeability of 40 D (200-300 μm).

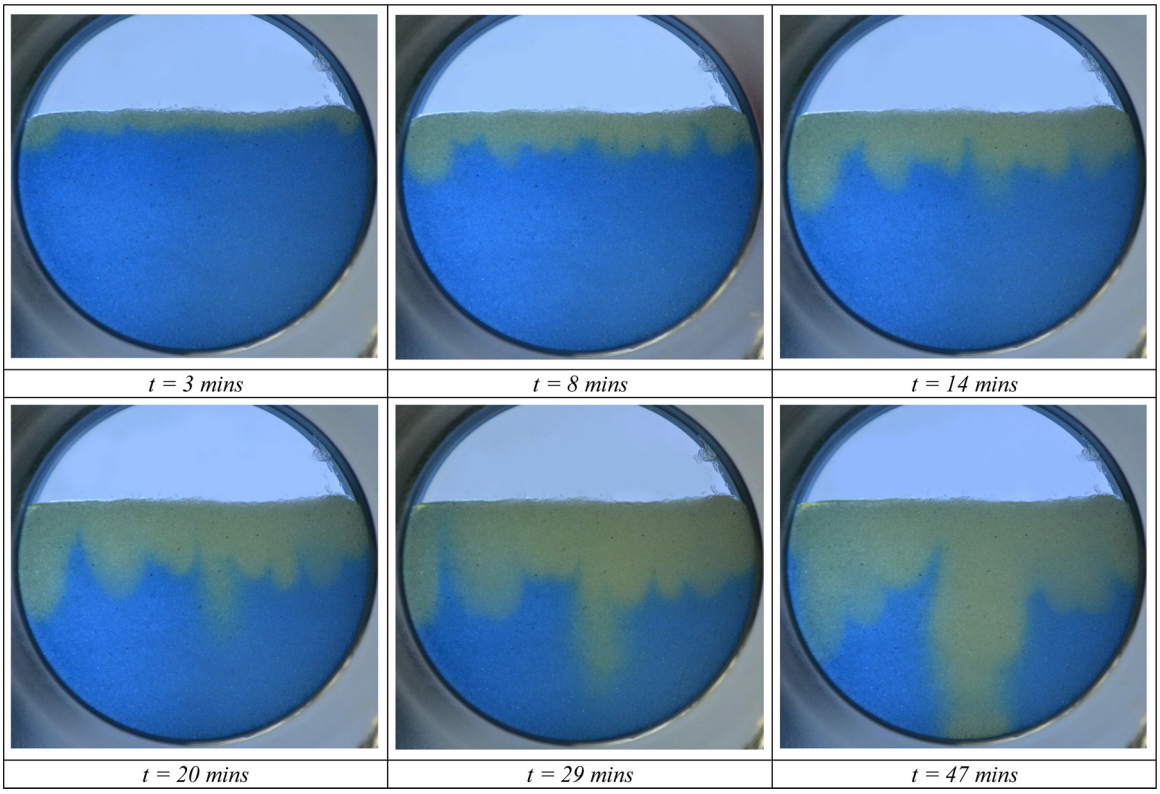

Fig. 13. Case 5; CO_2/Water system with porous medium with the permeability of 76 D (400-600 μm).

with time. When CO_2 fingering occurred, the length of the longest finger was considered. The graph shows that the CO_2 mixing rate increased with increasing permeability. The repeatability of the tests was found to be good. See the two tests (T-1 and T-2) for 4 D porous medium in Fig. 14. Vosper et al. (2014) have used the same beads size as of diameter 400 − 600 μm in their experiments at ambient conditions (1 bar/room temperature). They have reported that it took approximately 100 min. for CO_2 to reach a depth of 40 mm. The CO_2 transport rate is lower in their case due to the low pressure of CO_2. In our experiments (this study) when CO_2 is in supercritical state, we have calculated that it takes about 20 min.

In Fig. 15 average CO_2 flux velocity is given for different permeabilities. In Table 5 the time it took for CO_2 to reach the depth of 4 cm (t_{4cm}) is shown. From the results from both Fig. 15 and Table 5, it can be concluded that when the permeability is higher, the velocity is higher, i.e. the time taken to reach the depth of 4 cm is lower.

Eq. (5) shows the dimensionless time (τ) that has been used by (Farajzadeh et al., 2007) and (Faisal et al., 2015) to interpret the results from t_{4cm} with the Ra number.

$$\tau = \frac{D}{H^2} * t_{4cm} \tag{5}$$

Fig. 16 shows the relationship between Ra number and the dimensionless time (τ). Only experimental results from 4 D, 40 D, and 76 D porous media were selected for investigation since it was observed that in 500 mD porous medium CO_2 flow is more diffusion-driven than convection-driven as mentioned earlier. We have realized that the relationship between Ra number and scaled dimensionless time has a linear relationship.

3.3. Boundary effects

CO_2 was also observed to rise upward from the bottom with time, except in the 500 mD porous medium. Later the water with dissolved CO_2 from the top and bottom merged together. This can be seen at t = 1570 min in Fig. 11 and t = 145 min. in Fig. 12. CO_2 flow along the boundary of the cell has also been observed by Amarasinghe et al. (2018) at a lower pressure (10 bar) and room temperature conditions. Even though the boundary of this 2D cell cannot be seen from outside, it

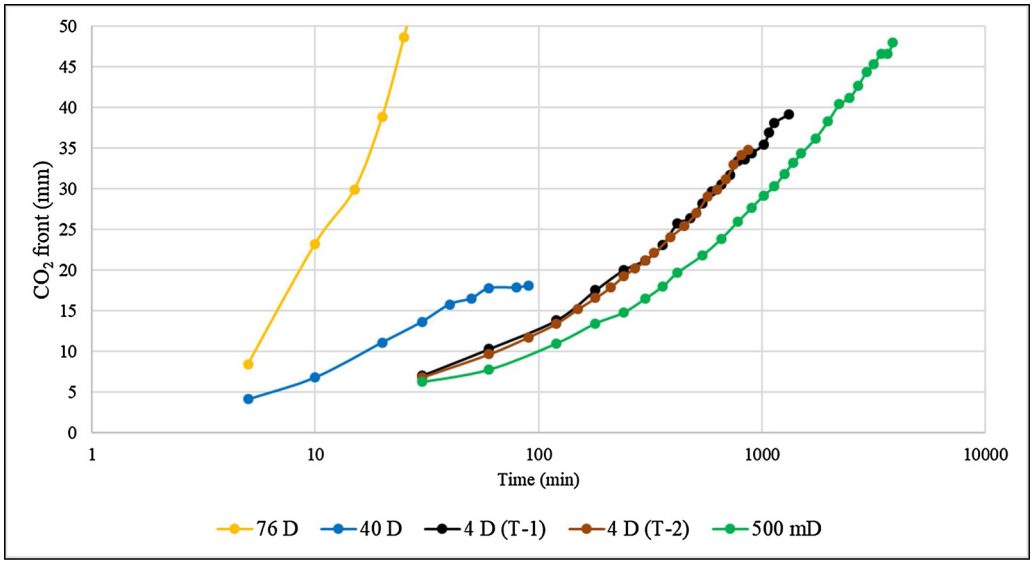

Fig. 14. Development of CO_2 front (length) downwards with time (log scale) for different permeable porous media. T-1 (Test 1) and T-2 (Test 2) denotes repeat tests for 4 D permeability porous medium.

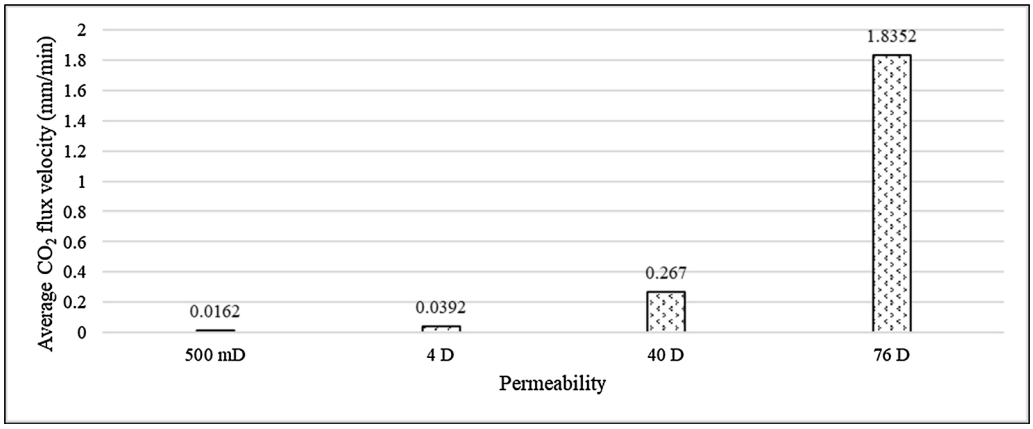

Fig. 15. Average CO_2 flux velocity vs permeability of porous media.

Table 5
Time taken for CO_2 to reach at 4 cm depth in the experiments.

Permeability	Time taken CO_2 to reach at 4 cm depth (t_{4cm})
No porous medium	25 s
500 mD	2220 min
4 D	1320 min
40 D	960 min
76 D	22 min

is probably the reason for CO_2 rising from the bottom at the end of the experiments. Vosper et al. (2014) also have seen high concentration of CO_2 alongside edges of the cell in their low-pressure experiments in a square arrangement. Generally, in a circular geometry boundary effects are more dominant compared to a square geometry.

4. Future work

Visualization of CO_2-mixing with different fluid phases (brine with different salinity and/or oil) and convection inside porous medium will be studied in the high-pressure Hele-Shaw cell, also at other experimental conditions. Moreover, geological heterogeneity is a big factor in the reservoir to initiate CO_2 instability inside porous medium. Hence, CO_2 convective mixing experiments will be carried out with different permeability layers (horizontally and vertically) using the same test cell to investigate the effects of heterogeneity. The findings from the experimental results will be used to fine-tune and upscale the available "The Open Porous Media (OPM)" simulator for large scale CO_2 storage.

5. Conclusions

The constructed high-pressure Hele-Shaw cell has made it possible to investigate CO_2-dissolution and mixing with water phases at pressures and temperatures realistic for reservoirs with CO_2-storage for the first time with porous medium. The CO_2 mixing and finger development in water phases without the presence of porous medium was extremely fast (seconds). The rate of CO_2 mixing in the porous media was found to increase with increasing permeability. The CO_2 dissolution pattern was observed to depend on the permeability. Fingering of CO_2-rich high-density water was observed in the highly permeable porous medium. Piston-like displacement was observed in lower permeable porous medium (500 mD). A linear relationship was obtained between Ra number and dimensionless time which can be used for scaling purposes and numerical analysis. Since it has visually observed that high permeable porous medium distributes CO_2 more easily, the results can be used in further understanding of optimum locations for injection of CO_2 in the field-scale applications to enhance the trapping.

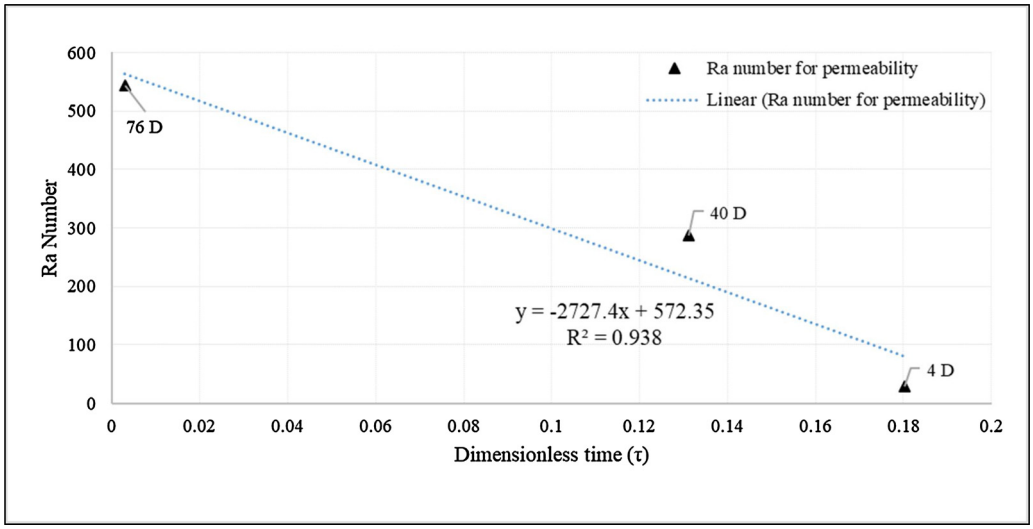

Fig. 16. Ra number vs dimensionless time for CO_2 convection driven flow in water saturated porous media.

CRediT authorship contribution statement

Widuramina Amarasinghe: Conceptualization, Methodology, Validation, Investigation, Writing, Visualization. **Ingebret Fjelde:** Conceptualization, Methodology, Validation, Investigation, Writing, Supervision, Funding acquisition. **Jan-Åge Rydland:** Conceptualization, Methodology, Resources, Writing. **Ying Guo:** Conceptualization, Methodology, Writing, Supervision, Project administration, Funding acquisition.

Declaration of Competing Interest

The authors declare that they have no known competing financial interests or personal relationships that could have appeared to influence the work reported in this paper.

Acknowledgments

The authors would like to thank the Research Council of Norway for the funding of this research project through the CLIMIT program which is dedicated to the accelerating and the commercialization of Carbon Capture and Storage (CCS) through research, development, and demonstration.

Appendix A. Supplementary data

Supplementary material related to this article can be found, in the online version, at doi:https://doi.org/10.1016/j.ijggc.2020.103082.

References

Agartan, E., Trevisan, L., Cihan, A., et al., 2015. Experimental study on effects of geologic heterogeneity in enhancing dissolution trapping if supercritical CO_2. Water Resour. Res. 51 (3), 1635–1648. https://doi.org/10.1002/2014WR015778.

Amarasinghe, W.S., Fjelde, I., Rydland, J.-A., et al., 2018. Design and testing of experimental set-up for investigation of convection during CO_2-transport in porous media. In: Presented at the 14th International Conference on Greenhouse Gas Control Technologies, GHGT-14. Melbourne, Australia. 21-26 October. . https://ssrn.com/abstract=3365918.

Bachu, S., 2008. CO_2 storage in geological media: role, means, status and barriers to deployment. Prog. Energy Combust. Sci. 34 (2), 254–273. https://doi.org/10.1016/j.pecs.2007.10.001.

Brock, W.R., Bryan, L.A., 1989. Summary results of CO_2 EOR field tests, 1972-1987. In: Presented at the Low Permeability Reservoirs Symposium. Denver, Colorado. 6-8 March. https://doi.org/10.2118/18977-MS.

Cadogan, S.P., Maitland, G.C., Trusler, J.P.M., 2014. Diffusion coefficients of CO_2 and N_2 in water at temperatures between 298.15 K and 423.15 K at pressures up to 45 MPa. J. Chem. Eng. Data 59 (2), 519–525. https://doi.org/10.1021/je401008s.

Celia, M.A., Bachu, S., Nordbotten, J.M., et al., 2015. Status of CO_2 storage in deep saline aquifers with emphasis on modeling approaches and practical simulations. Water Resour. Res. 51 (9), 6846–6892. https://doi.org/10.1002/2015WR017609.

Efika, E.C., Hoballah, R., Li, X., et al., 2016. Saturated Phase Densities of (CO_2+H_2O) at Temperatures from (293 to 450)K and Pressures up to 64MPa. J. Chem. Thermodyn. 93, 347–359. https://doi.org/10.1016/j.jct.2015.06.034.

Emami-Meybodi, H., Hassanzadeh, H., Green, C.P., et al., 2015. Convective dissolution of CO_2 in saline aquifers: progress in modeling and experiments. Int. J. Greenh. Gas Control. 40 (Supplement C), 238–266. https://doi.org/10.1016/j.ijggc.2015.04.003.

Faisal, T.F., Chevalier, S., Bernabe, Y., et al., 2015. Quantitative and qualitative study of density driven CO_2 mass transfer in a vertical hele-shaw cell. Int. J. Heat Mass Transf. 81 (Supplement C), 901–914. https://doi.org/10.1016/j.ijheatmasstransfer.2014.11.017.

Fang, F., Babadagli, T., 2016. 3-d visualization of diffusive and convective solvent transport processes in oil-saturated porous media using laser technology. J. Vis. 19 (4), 615–629. https://doi.org/10.1007/s12650-016-0350-1.

Farajzadeh, R., Salimi, H., Zitha, P.L.J., et al., 2007. Numerical simulation of density-driven natural convection in porous media with application for CO_2 injection projects. Int. J. Heat Mass Transf. 50 (25), 5054–5064. https://doi.org/10.1016/j.ijheatmasstransfer.2007.08.019.

Freund, P., Ormerod, W.G., 1997. Progress toward storage of carbon dioxide. Energy Convers. Manage. 38, S199–S204. https://doi.org/10.1016/S0196-8904(96)00269-5.

Hartline, B.K., Lister, C.R.B., 1977. Thermal convection in a hele-shaw cell. J. Fluid Mech. 79 (2), 379–389. https://doi.org/10.1017/S0022112077000202.

Hebach, A., Oberhof, A., Dahmen, N., 2004. Density of water + carbon dioxide at elevated pressures: measurements and correlation. J. Chem. Eng. Data 49 (4), 950–953. https://doi.org/10.1021/je034260i.

Héricz, D., Sarkadi, T., Erdei, G., et al., 2017. Simulation of small- and wide-angle scattering properties of glass-bead retroreflectors. Appl. Opt. 56, 3969. https://doi.org/10.1364/AO.56.003969.

Holm, L.W., 1982. CO_2 flooding: its time has come. J. Pet. Technol. 34 (12), 2739–2745. https://doi.org/10.2118/11592-PA.

IPCC, 2005. IPCC Special report on carbon dioxide capture and storage. In: Prepared by Working Group III of the Intergovernmental Panel on Climate Change Cambridge. United Kingdom and New York. . https://www.cambridge.org/ch/academic/subjects/earth-and-environmental-science/climatology-and-climate-change/carbon-dioxide-capture-and-storage-special-report-intergovernmental-panel-climate-change?format=HB&isbn=9780521866439.

Khosrokhavar, R., Elsinga, G., Farajzadeh, R., et al., 2014. Visualization and investigation of natural convection flow of CO_2 in aqueous and oleic systems. J. Pet. Sci. Eng. 122 (Supplement C), 230–239. https://doi.org/10.1016/j.petrol.2014.07.016.

Kneafsey, T.J., Pruess, K., 2010. Laboratory flow experiments for visualizing carbon dioxide-induced, density-driven brine convection. Transp. Porous Media 82 (1), 123–139. https://doi.org/10.1007/s11242-009-9482-2.

Kneafsey, T.J., Pruess, K., 2011. Laboratory experiments and numerical simulation studies of convectively enhanced carbon dioxide dissolution. Energy Procedia 4 (Supplement C), 5114–5121. https://doi.org/10.1016/j.egypro.2011.02.487.

Kuuskraa, V.A., Godec, M.L., Dipietro, P., 2013. CO_2 utilization from "Next generation" CO_2 enhanced oil recovery technology. Energy Procedia 37, 6854–6866. https://doi.org/10.1016/j.egypro.2013.06.618.

Lin, H., Fujii, T., Takisawa, R., et al., 2008. Experimental evaluation of interactions in supercritical CO_2/Water/Rock minerals system under geologic CO_2 sequestration conditions. J. Mater. Sci. 43 (7), 2307–2315. https://doi.org/10.1007/s10853-007-2029-4.

Lindeberg, E., Wessel-Berg, D., 1997. Vertical convection in an aquifer column under a gas cap of CO_2. Energy Convers. Manage. 38, S229–S234. https://doi.org/10.1016/S0196-8904(96)00274-9.

Liyanage, R., Crawshaw, J., Krevor, S., et al., 2017. Multidimensional imaging of density driven convection in a porous medium. Energy Procedia 114 (Supplement C), 4981–4985. https://doi.org/10.1016/j.egypro.2017.03.1641.

Lu, G., Liu, Y., Jiang, L., et al., 2017. Study of density driven convection in a hele-shaw cell with application to the carbon sequestration in aquifers. Energy Procedia 114 (Supplement C), 4303–4312. https://doi.org/10.1016/j.egypro.2017.03.1576.

Lv, P., Liu, Y., Jiang, L., et al., 2016. Experimental determination of wettability and heterogeneity effect on CO_2 distribution in porous media. Greenh. Gases Sci. Technol. 6 (3), 401–415. https://doi.org/10.1002/ghg.1572.

Lv, P., Liu, Y., Chen, J., et al., 2017. Pore-scale investigation of effects of heterogeneity on CO_2 geological storage using stratified sand packs. Greenh. Gases Sci. Technol. 7 (6), 972–987. https://doi.org/10.1002/ghg.1702.

Mahmoodpour, S., Rostami, B., Soltanian, M.R., et al., 2019. Effect of brine composition on the onset of convection during CO_2 dissolution in brine. Comput. Geosci. 124, 1–13. https://doi.org/10.1016/j.cageo.2018.12.002.

Mojtaba, S., Behzad, R., Rasoul, N.M., et al., 2014. Experimental study of density-driven convection effects on CO_2 dissolution rate in formation water for geological storage. J. Nat. Gas Sci. Eng. 21 (Supplement C), 600–607. https://doi.org/10.1016/j.jngse.2014.09.020.

Neufeld, J.A., Hesse, M.A., Riaz, A., et al., 2010. Convective dissolution of Carbon Dioxide in saline aquifers. Geophys. Res. Lett. 37 (22). https://doi.org/10.1029/2010GL044728.

Outeda, R., Hasi, C.E., D'Onofrio, A., et al., 2014. Experimental study of linear and nonlinear regimes of density-driven instabilities induced by CO_2 dissolution in water. Chaos Interdiscip. J. Nonlinear Sci. 24 (1), 013135. https://doi.org/10.1063/1.4868040.

Roefs, P., Moretti, M., Welkenhuysen, K., et al., 2019. CO_2-enhanced oil recovery and CO_2 capture and storage: an environmental economic trade-off analysis. J. Environ. Manage. 239, 167–177. https://doi.org/10.1016/j.jenvman.2019.03.007.

Rueden, C.T., Schindelin, J., Hiner, M.C., et al., 2017. ImageJ2: ImageJ for the next generation of scientific image data (in eng). BMC Bioinformatics 18 (1), 529. https://doi.org/10.1186/s12859-017-1934-z.

SigmundLindner SiLibeads SOLID Micro Glass Beads - Product data sheet. Germany. 2019-03-04. https://www.sigmund-lindner.com/wp-content/uploads/2018/08/PDS-en-SiLibeads-SOLID-Micro-Glass-Beads.pdf.

Sohrabi, M., Riazi, M., Jamiolahmady, M., et al., 2009. Enhanced oil recovery and CO_2 storage by carbonated water injection. In: Presented at the International Petroleum Technology Conference. Doha, Qatar. 2009/1/1/. https://doi.org/10.2523/IPTC-14070-ABSTRACT.

Song, Y., Nishio, M., Chen, B., et al., 2003. Measurement on CO_2 solution density by optical technology. J. Vis. 6 (1), 41–51. https://doi.org/10.1007/bf03180963.

Soroush, M., Wessel-Berg, D., Torsaeter, O., et al., 2012. Affecting parameters in density driven convection mixing in CO_2 storage in brine. In: Presented at the SPE Europec/EAGE Annual Conference. Copenhagen, Denmark. 4-7 June. https://doi.org/10.2118/154901-MS.

Taheri, A., Torsaeter, O., Wessel-Berg, D., et al., 2012. Experimental and simulation studies of density-driven-convection mixing in a hele-Shaw geometry with application for CO_2 sequestration in brine aquifers. In: Presented at the SPE Europec/EAGE Annual Conference. Copenhagen, Denmark. 4-7 June. https://doi.org/10.2118/154908-MS.

Taheri, A., Torsæter, O., Lindeberg, E., et al., 2018. Qualitative and quantitative experimental study of convective mixing process during storage of CO_2 in heterogeneous saline aquifers. Int. J. Greenh. Gas Control. 71, 212–226. https://doi.org/10.1016/j.ijggc.2018.02.003.

Tang, Y., Li, Z., Wang, R., et al., 2019. Experimental study on the density-driven carbon dioxide convective diffusion in formation water at reservoir conditions. ACS Omega 4 (6), 11082–11092. https://doi.org/10.1021/acsomega.9b00627.

Teng, Y., Jiang, L., Fan, Y., et al., 2017. Quantifying the dynamic density driven convection in high permeability packed beds. Magn. Reson. Imaging 39, 168–174. https://doi.org/10.1016/j.mri.2017.03.004.

Teng, Y., Wang, P., Liu, Y., et al., 2018. A spectrophotometric method for measuring dissolved CO_2 in saline water. Exp. Fluids 59 (9), 138. https://doi.org/10.1007/s00348-018-2594-0.

Thomas, C., Lemaigre, L., Zalts, A., et al., 2015. Experimental study of CO_2 convective dissolution: the effect of color indicators. Int. J. Greenh. Gas Control. 42 (Supplement C), 525–533. https://doi.org/10.1016/j.ijggc.2015.09.002.

Thomas, C., Dehaeck, S., De Wit, A., 2018. Convective dissolution of CO_2 in water and salt solutions. Int. J. Greenh. Gas Control. 72, 105–116. https://doi.org/10.1016/j.ijggc.2018.01.019.

Trykkbeholderkomite, D.N., 1986. Generelle Regler for Trykkbeholdere. chapter 5.2. Norsk verkstedsindustris standardiseringssentral.

Tsai, P.A., Riesing, K., Stone, H.A., 2013. Density-driven convection enhanced by an inclined boundary: implications for geological CO_2 storage (in eng). Phys. Rev. E Stat. Nonlin. Soft Matter Phys. 87 (1), 011003. https://doi.org/10.1103/PhysRevE.87.011003.

United Nations, 2015. The Paris Agreement. https://unfccc.int/sites/default/files/english_paris_agreement.pdf.

Vosper, H., Kirk, K., Rochelle, C., et al., 2014. Does numerical modelling of the onset of dissolution-convection reliably reproduce this key stabilization process in CO_2 storage? Energy Procedia 63, 5341–5348. https://doi.org/10.1016/j.egypro.2014.11.566.

Vreme, A., Nadal, F., Pouligny, B., et al., 2016. Gravitational instability due to the dissolution of Carbon Dioxide in a hele-shaw cell (in english). Phys. Rev. Fluids 1 (6), 064301. https://doi.org/10.1103/PhysRevFluids.1.064301.

Wang, L., Hyodo, A., Sakai, S., et al., 2016. Three-dimensional visualization of natural convection in porous media. Energy Procedia 86 (Supplement C), 460–468. https://doi.org/10.1016/j.egypro.2016.01.047.

Zhang, D., Song, J., 2014. Mechanisms for geological carbon sequestration. Procedia IUTAM 10, 319–327. https://doi.org/10.1016/j.piutam.2014.01.027.

Zhao, Y., Song, Y., Liu, Y., et al., 2011. Visualization and measurement of CO_2 flooding in porous media using MRI. Ind. Eng. Chem. Res. 50 (8), 4707–4715. https://doi.org/10.1021/ie1013019.